Journal of Materials Chemistry A

ROYAL SOCIETY OF CHEMISTRY

PAPER

View Article Online
View Journal | View Issue

Check for updates

Cite this: J. Mater. Chem. A, 2026, 14, 7502

Passive multistage solar desalination enables durable high-efficiency freshwater production

Wenzong Li,[a] Tianyi Ma,[b] Xu Wang,[a] Lemin Zhang,[a] Wenna Ge,[a] Chenguang Lu,[a] Xiangge Bai,[a] Jiahui Chu,[a] Zichao Yuan,[a] Shile Feng [a] and Yahua Liu *[ac]

Received 5th November 2025
Accepted 6th January 2026

DOI: 10.1039/d5ta08988c

rsc.li/materials-a

Solar desalination presents a sustainable solution to global water scarcity, with reverse multistage distillation systems offering particularly high efficiency. The hydrophilic wick, serving as the evaporation interface in reverse multistage distillation systems, is an essential component. However, conventional hydrophilic layers suffer from low thermal conductivity and salt accumulation, which undermine long-term efficiency and operational stability. Here, we report a *Volutharpa ampullacea perryi*-inspired interface, featuring an aluminum-based superhydrophilic surface integrated with glass fiber conduits. This architecture enables rapid, directional transport of micron-scale liquid films, suppressing localized salt crystallization while reducing evaporation heat transfer due to the low thermal conductivity of glass fibers. Under one sun illumination, the system achieves a record solar-to-steam efficiency of 410% and a freshwater production rate of 6.25 kg m^{-2} h^{-1} and meanwhile retains stable operation without salt accumulation over extended periods. These results establish a new paradigm for solar desalination with scalable, efficient, and salt-resistant freshwater collection for global water-stressed regions.

1 Introduction

The escalating global demand for freshwater, fuelled by rapid economic development and population growth, has left two-thirds of the global population facing water scarcity.[1–5] Seawater, the most abundant water resource on Earth, presents a viable solution through desalination.[6,7] However, conventional desalination methods, such as electricity-driven reverse osmosis and thermal desalination, are highly energy-intensive and contribute significantly to greenhouse gas emissions.[8–10] Solar-driven steam generation has recently gained attention as a sustainable alternative due to its energy-free operation and minimal carbon footprint.[11–13] Among these technologies, solar-driven interfacial desalination has emerged as a promising strategy to address water scarcity.[14–16]

Traditional solar-driven interfacial desalination systems consist of a solar absorber, which converts sunlight into heat to generate steam, and a thermal insulator, which minimizes heat loss by localizing thermal energy at the surface.[17,18] These systems often suffer from seawater infiltration, which reduces solar absorption by increasing surface reflectivity.[19,20] Another key limitation lies in the freshwater collection system, typically a closed structure with a transparent cover that allows sunlight transmission and vapor condensation. However, steam condensation on the cover reduces light transmittance and increases reflectivity, leading to solar energy losses of up to 35%.[21] Recently, solar-driven reverse multistage desalination has demonstrated significant advancements in seawater purification, offering higher evaporation rates and superior solar-to-water conversion efficiency.[22,23] Unlike conventional interface desalination, this approach separates light absorption and condensation regions, enhancing solar energy capture and enabling latent heat recovery.[24,25] This configuration supports the development of multistage evaporation systems, significantly boosting efficiency.[15]

Typically, a solar-driven reverse multistage evaporation system comprises several key components, including a photothermal layer, heat transfer layer, hydrophilic layer, and condensation layer.[26–29] Among these, the hydrophilic layer plays a crucial role by ensuring continuous seawater replenishment and sustaining evaporation efficiency. Note that, current hydrophilic layers made from paper or cellulose exhibit poor thermal conductivity, while metal-based alternatives, though conductive, suffer from rapid salt accumulation due to inefficient brine discharge.[30] Therefore, effective salt rejection and discharge remain critical challenges for the sustainability of metal-based reverse desalination systems.[31–33]

In this study, we address these challenges through a biomimetic approach inspired by the water transport mechanisms of *Volutharpa ampullacea perryi*. We developed an aluminium-based reverse desalination device featuring superhydrophilic microscale V-groove arrays (SMVAs). These grooves enhance

[a]State Key Laboratory of High-performance Precision Manufacturing, Dalian University of Technology, Dalian 116024, P. R. China. E-mail: yahualiu@dlut.edu.cn
[b]Library, Dalian University of Technology, Dalian 116024, P. R. China
[c]Department of Anaesthesiology, Central Hospital of Dalian University of Technology, Dalian 116033, P. R. China

capillary-driven water flow, enabling rapid salt rejection and improved heat transfer for enhanced evaporation efficiency. Paired with flexible superhydrophilic glass fibres for continuous seawater supply and drainage, the system achieves a solar-to-steam efficiency of 410% with a freshwater production rate of 6.25 kg m^{-2} h^{-1} under one sun illumination. By eliminating low-conductivity materials and supporting up to 15 evaporation stages, this design offers a scalable, efficient solution for sustainable freshwater production.

2 Results and discussion

2.1 Preparation and characterization of SMVAs

Marine gastropods can resist turbulent flows through surface-grown microgroove structures. Fig. 1a–c show the optical and scanning electron microscopy (SEM) images of *Volutharpa ampullacea perryi*, whose surface is densely covered with microgrooves approximately 150 μm wide and 100 μm deep. These structures promote rapid seawater transport along the groove walls (Fig. 1d and Video S1). Inspired by this natural architecture, we fabricated SMVAs *via* picosecond laser etching (Fig. S1). Briefly, superhydrophilic micro-scale V-groove arrays were fabricated on 500 μm-thick aluminum sheets using a picosecond laser with a wavelength of 1060 nm.[34–36] The SEM image shows microgrooves of 100 μm width (Fig. 1e) and 40 μm depth (Fig. S2). The enlarged view further presents nested subgrooves within the primary grooves, with their surface covered by a porous nanostructured layer (Fig. S3). Energy dispersive spectroscopy (EDS) analysis confirms that SMVAs comprise aluminum and oxygen, with the Al content significantly exceeding oxygen content (Fig. S4), indicating a composite surface of metallic aluminum and aluminum oxide. Additional X-ray photoelectron spectroscopy (XPS) spectra corroborate this composition:[37] major peaks at 531.48 eV (O 1s) and 74.48 eV (Al 1s) correspond to oxygen and aluminum, while deconvoluted peaks at 532.38 eV (–OH), 530.88 eV (C═O), 74.78 eV (AlO_x), and 73.58 eV (Al–Al bonds) confirm hydroxylation, surface oxidation, and metallic bonding states (Fig. S5).

The microgrooves function as capillary channels, enabling the rapid upward movement of water droplets from the base (Fig. 1f).[38,39] The advancing water front height H with time (t), follows the Washburn–Rideal eqn (1).

$$H^2 = K(\alpha, \theta)\frac{\gamma h}{\mu}t \quad (1)$$

where γ is the liquid surface tension, μ is the bulk liquid viscosity, h is the microgroove depth and $K(\alpha,\theta)$ is a geometric factor dependent on the groove angle α and the liquid/surface contact angle θ. To measure the water rise height, we vertically mounted the sample and placed a 5 μL water droplet at its base, recording the time-dependent progression of H using a high-speed camera (Fig. 1g). The water climbs against gravity with an initial velocity of 156 mm s^{-1} before stabilizing at a steady-state velocity of ~41 mm s^{-1} upon reaching a height of 22 mm. The results align well with the classical Washburn

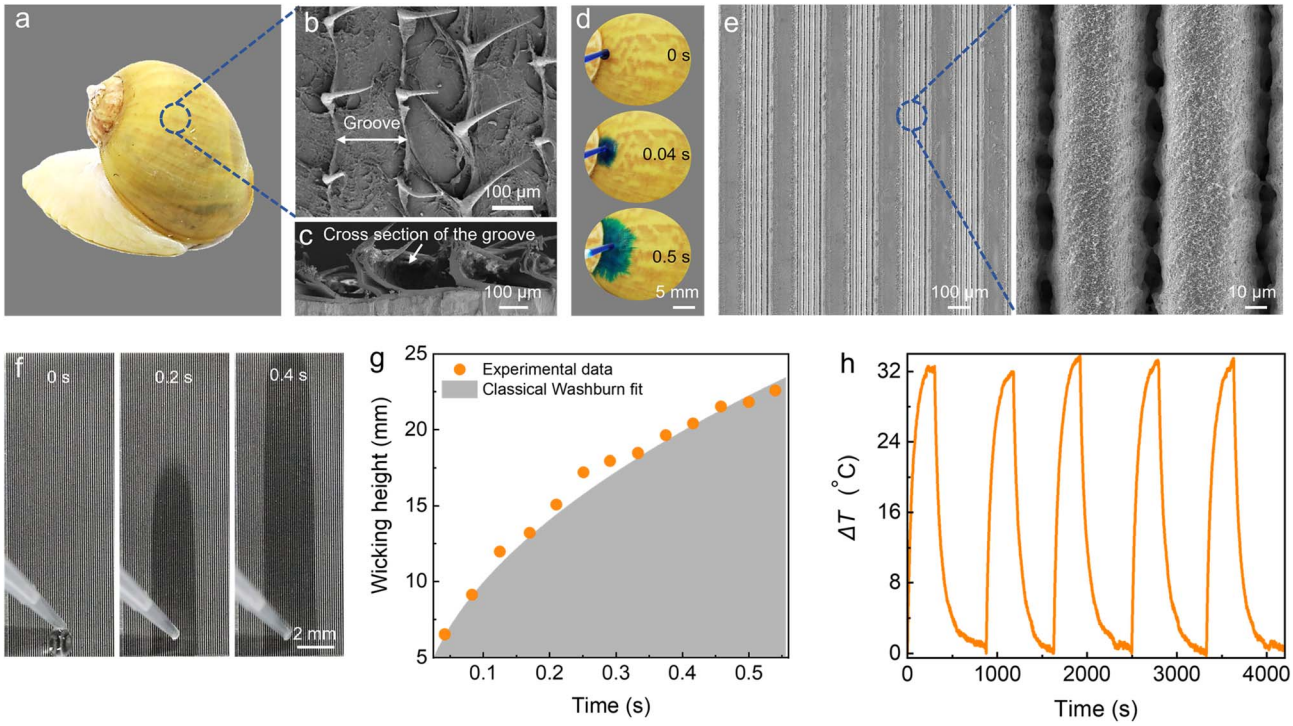

Fig. 1 Characterization of the bioinspired superhydrophilic aluminum surface with V-grooves. (a) Optical image of *Volutharpa ampullacea perryi* and (b) Surface SEM image of the shell. (c) Cross sectional SEM image of the shell. (d) Water absorption capability of the shell surface. (e) SEM images of the V-groove structure of SMVAs at low and high magnifications. (f) Image sequences of the wicking behavior of a water droplet on the SMVAs. (g) The water wet-front (H) propagation *versus* time, fitted with Washburn fit. (h) The cyclic temperature variation curves of the SMVAs under one sun illumination.

model, confirming that $H^2 \propto t$. For comparison, we fabricated a superhydrophilic aluminum surface (SAS) without V-grooves. Water absorption on the SAS was significantly slower, requiring approximately 34 s to rise 20 mm (Fig. S6a). The SMVAs, however, supported a water rise in excess of 170 mm, albeit with a notable decrease in flow velocity at greater heights (Fig. S6b).

Moreover, the SMVAs exhibit superior heat transfer efficiency compared to smooth aluminum. Under one sun illumination, they heat up more rapidly, reaching a maximum temperature increase ΔT of 32 °C (Fig. S7 and Note S1). Thermal stability was assessed through five on/off illumination cycles using a solar simulator (Fig. 1h). After five cycles, ΔT stabilized at 32 °C within 200 s, demonstrating excellent thermal transfer stability. With their enhanced heat transfer properties, SMVAs also facilitate rapid liquid evaporation (Fig. S8 and Note S2).

2.2 Performance of a single-stage evaporator using SMVAs

To optimize performance, three different types of single-stage evaporators based on SMVAs were designed (Fig. 2a) and their evaporation performance was evaluated under identical illumination. In SMVAs-A, water is supplied to the evaporation interface *via* direct contact with the SMVAs, whereas SMVAs-B and SMVAs-C employ flexible superhydrophilic glass fibers (FSGF) of low thermal conductivity for water transport. The water absorption capability of superhydrophilic glass fibers is shown in Fig. S9. Compared with SMVAs-A and SMVAs-B, SMVAs-C incorporates a multilayer photothermal interface consisting of a solar-transparent polymethyl methacrylate (PMMA) layer, an air-based thermal insulation layer, and a solar absorber. Detailed information on the fabrication procedure and photothermal performance of the solar absorber is provided in Note S3. To ensure a high flow velocity along the SMVAs, we employed FSGF as the drainage component of the evaporator. In contrast to the rigid SMVAs, the FSGF can droop freely, allowing seawater to continuously infiltrate and ultimately reach the concentrated brine tank through a combination of capillary action and gravity (Fig. S12).

We next evaluated the solar vapor generation performance of three single-stage evaporators under constant 1 kW m^{-2} irradiation by monitoring time-dependent water mass loss. As shown in Fig. 2b, mass change curves for the three evaporators and a bare water surface reveal that SMVAs-C significantly outperforms the others, achieving a notably higher evaporation rate. Evaporation rates were calculated from the slopes of these curves, with SMVAs-C of area 6 cm^2 reaching 1.31 kg m^{-2} h^{-1} under one sun illumination (dot in Fig. 2c). Solar-to-steam efficiency (η) was calculated using the equation[40]

$$\eta = mh_v/C_{opt}P_o \quad (2)$$

where m is the net evaporation rate, h_v is the evaporation enthalpy of water in the SMVAs (2350 J g^{-1}), P_o is the solar irradiation power and C_{opt} is the optical concentration (Note S4). As indicated by the columnar in Fig. 2c, SMVAs-C achieved a solar-to-steam efficiency of approximately 83% under one sun illumination, outperforming the other designs. Despite the continuous high-speed water flow on the SMVAs, the flow

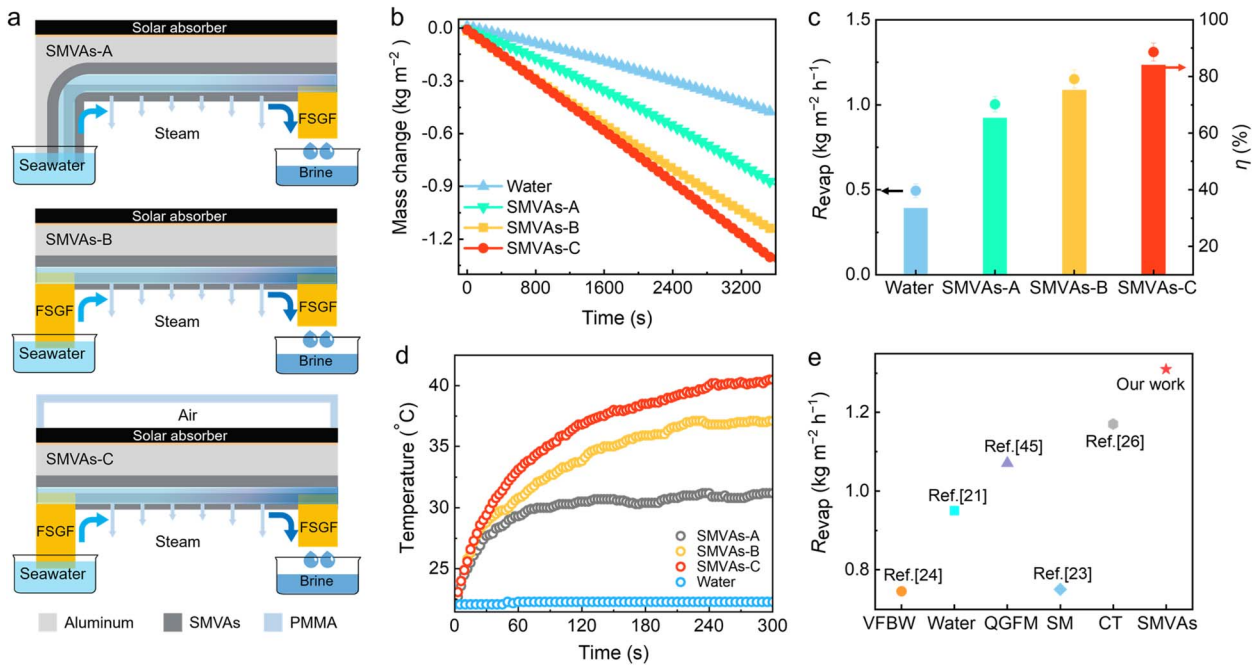

Fig. 2 Fabrication and performance evaluation of different types of primary evaporators. (a) Schematic illustration of the structural design and evaporation mechanism of different types of evaporators. (b) Time-dependent mass variation of water for different evaporator types under one sun illumination. (c) Evaporation rate and solar-to-steam efficiency of different types of evaporators under one sun illumination. (d) Temporal variation of the evaporation interface temperature for different evaporator types under one sun illumination. (e) Comparison of evaporation rates with previously reported values.

thickness remains sub-micron (Fig. S13), resulting in an extremely low volumetric flow rate that minimizes thermal losses (Note S5). The contact thermocouple measurements (Fig. 2d) show that SMVAs-C rapidly reaches an evaporation interface temperature of 40.5 °C—higher than those of SMVAs-B (37.1 °C) and SMVAs-A (31.2 °C) under identical conditions.

Interestingly, the top surface and bulk water temperatures of SMVAs-C remain lower than those of the other evaporators due to the presence of an air insulation layer and the low thermal conductivity (0.04 W m^{-1} K^{-1}) of the hydrophilic fibers. These features effectively reduce heat loss through convection and conduction (Fig. S15), yielding calculated losses of ~0.9% (conduction), ~2.5% (radiation), ~7.25% (convection), and ~3% (dissipation to the water phase) (Note S6). Furthermore, the high thermal conductivity of SMVAs enables rapid interfacial temperature increase, as confirmed by hot plate tests (Fig. S16a) where SMVAs reached higher steady-state temperatures faster than glass fibers. The thermal conductivity measurements indicate that the SMVAs achieve values of up to 220 W m^{-1} K^{-1} (Fig. S16b and Note S7). Consequently, SMVAs-C achieves superior evaporation rates compared to low-thermal-conductivity alternatives (Fig. 2e).

2.3 Salt-rejection performance and durability of SMVAs-C in desalination

Effective salt rejection is essential for sustainable solar desalination.[41–43] To demonstrate that the high-flow surface of SMVAs-C can prevent salt crystallization, we used SAS, a superhydrophilic aluminum surface without V-grooves, to fabricate a low flow velocity C-type evaporator. Under one sun illumination, the corresponding water mass change results for different flow-velocity evaporators are presented in Fig. 3a. The evaporation rate of SAS-C gradually declined and stabilized at approximately 0.96 kg m^{-2} h^{-1}, markedly lower than that of SMVAs-C (1.31 kg m^{-2} h^{-1}). In addition, continuous evaporation tests under one sun illumination confirm the excellent stability of SMVAs-C during seawater purification. Even after 10 hours of uninterrupted operation, the evaporation interface remains free of salt crystallization, demonstrating both effective salt rejection and long-term usability (Fig. 3b and Video S2). In contrast, the low-flow C-type evaporator (SAS-C) exhibited visible salt crystallization within 15 min and became almost completely fouled after 1.2 h, severely impeding vapor escape and reducing performance (Fig. 3c and Video S2).

To systematically evaluate salt tolerance, we tested SMVAs-C with solutions of varying salinity: ultrapure water (0 wt%), seawater (2.8 wt%), and saline solutions of 7 wt%, 10 wt%, 15 wt% and 20 wt%. As shown in Fig. 3d, the evaporation rate decreased slightly with increasing salinity, yielding 1.336, 1.31, 1.27, 1.15, 1.09 and 1.02 kg m^{-2} h^{-1}, respectively. Despite the higher salt concentration, the 20 wt% brine retained a stable evaporation rate (Fig. S17), underscoring the salt-resistance of SMVAs-C. This performance is attributed to its high water transport capacity, enabling an upward brine flow velocity of 29.1 mm s^{-1} against gravity (Fig. 3e), which efficiently removes concentrated brine to sustain high evaporation rate.

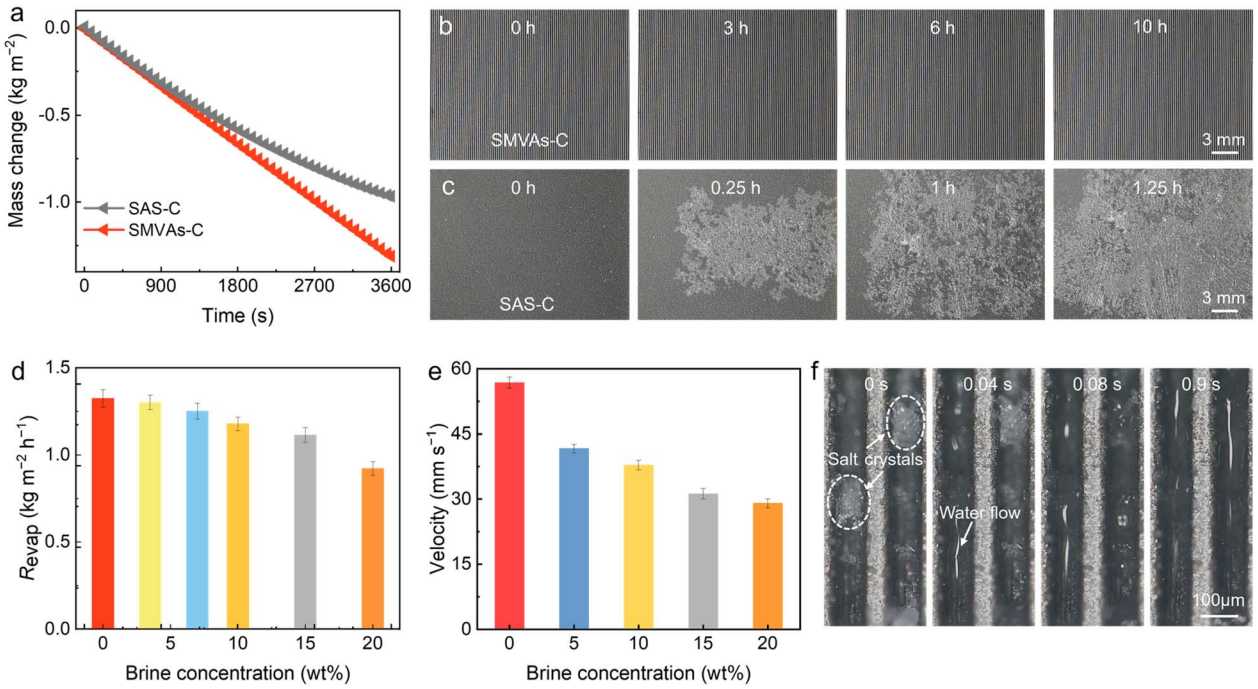

Fig. 3 Salt rejection mechanism of the SMVAs-C evaporator induced by high flow velocity. (a) Mass change of seawater on evaporators with high and low flow velocities under one sun illumination. Optical images of the continuous solar desalination process on evaporators with high (b) and low (c) flow velocities using seawater as the bulk water source. (d) Evaporation rate for SMVAs-C evaporator using feedwater with different salinities under one sun illumination. (e) Water transport velocity of the SMVAs-C for the water with different salinities. (f) Time sequences of optical images of rapid dissolution of NaCl solid crystals at high flow rates.

Moreover, the high flow velocity at the SMVAs-C interface accelerates the dissolution of surface salt crystals. As shown in Fig. 3f, salt crystals within V-shaped grooves dissolve completely within 0.9 s due to the rapid water flow. To further verify this capacity, 20 mg of NaCl crystals were manually added to the SMVAs-C surface during seawater evaporation under one sun illumination. The salt crystals began dissolving immediately upon contact with seawater and fully disappeared within 20 min (Fig. S18 and Video S3), confirming the system's strong salt-dissolution ability.

2.4 Design and performance analysis of multistage reverse-distillation devices

To maximize freshwater yield per solar absorption area, we developed a multistage passive solar desalination apparatus (MPSDA) based on SMVAs and condensation enthalpy recovery (Fig. 4a).[44,45] The system features 3D-printed single-stage evaporation frames (2 mm thick) that integrate the SMVAs and the water supply/drainage. This innovative design combines hydrophilic and thermal exchange functions within a single layer: the SMVA upper surface serves as the evaporation interface while the lower surface acts as the condensation heat-transfer layer, enabling an ultra-compact 30 mm total device thickness (Fig. S19). Fig. 4b illustrates the working principle of the MPSDA. In each stage, the interfacial air layer acts as both a thermal insulator and a vapor transport medium, accelerating vapor delivery to the condensation layer and improving condensation efficiency. The top surface of this layer is covered with superhydrophilic glass fibers, which quickly absorb condensate droplets and drain them downward under gravity, enabling effective water collection.

Systematic evaluation of stage number effects revealed significant performance improvements. As shown in Fig. 4c, mass change increases with stage count due to the utilization of condensation enthalpy from the vapor generated at each level. As the number of stages (n) increases from 1 to 15, the evaporation rate rises from 1.31 to 6.25 kg m^{-2} h^{-1}, and the solar-to-steam efficiency improves from 189% to 410% under one sun illumination (Fig. 4d). The nonlinear efficiency growth stems from heat losses due to imperfect sealing, with first-stage measurements showing 69% freshwater recovery and 31% vapor loss (Fig. S20). To investigate this performance enhancement, we performed real-time thermal profiling of each stage using contact thermocouples. As shown in Fig. 4e, under one sun illumination for 1.5 h, the first-stage temperature rose rapidly to 45 °C within 500 s and stabilized at 50 °C. Thanks to the high thermal conductivity of SMVAs and the minimal thickness of each evaporator stage, the temperature drop between the first and third stages is just 8.5 °C, and only 22 °C between the first and fifteenth stages. This small gradient indicates efficient vertical heat transfer throughout the stack and minimal lateral heat loss, thereby boosting overall evaporation performance. The detailed mechanism of high evaporation performance is provided in Note S8. Consequently, the MPSDA demonstrates superior performance across five key metrics compared to previously reported solar distillation technologies (Fig. 4f).

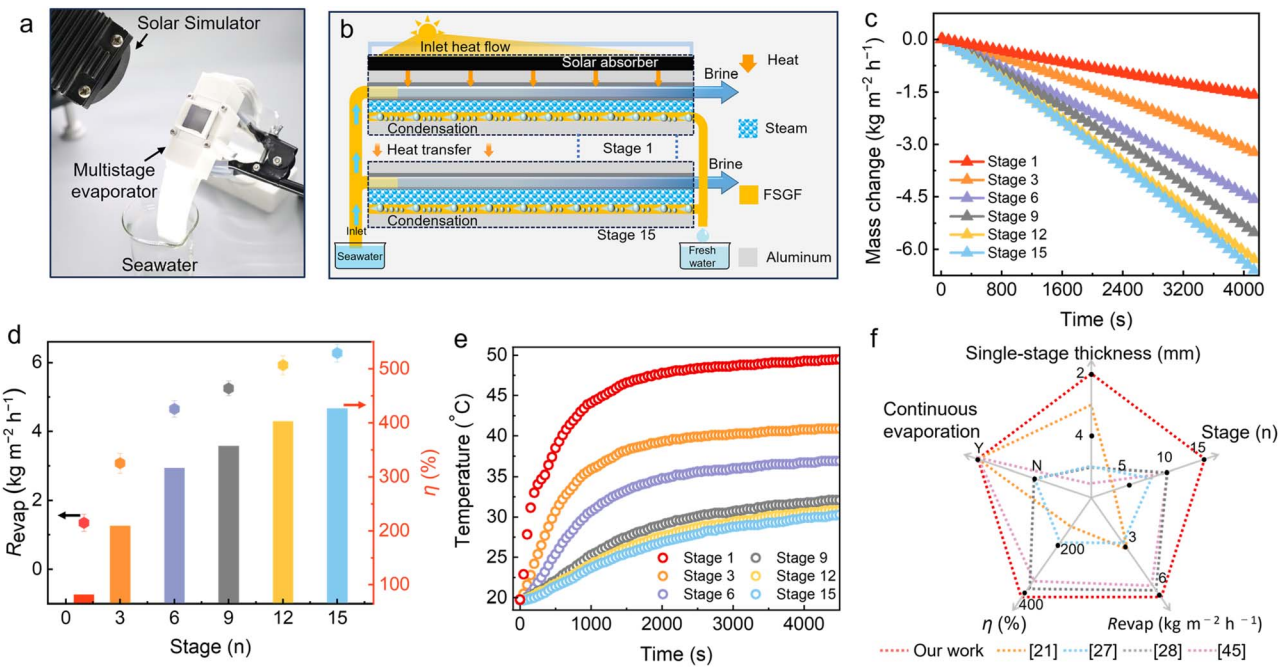

Fig. 4 Solar evaporation performance under controlled indoor conditions. (a) Photograph of the indoor experimental setup. (b) Schematic diagram of the MPSDA operating in low-salinity water mode. (c) Mass variation of the MPSDA with different stages under one sun illumination. (d) Evaporation rate and solar-to-steam efficiency of the MPSDA with different stages under one sun illumination. (e) Temperature evolution across different stages during a 1.5 h test. (f) The notable advantages of MPSDA on the passive multi-stage evaporation system compared with other techniques from five aspects. Y, yes; N, no.

2.5 Outdoor solar desalination

While indoor testing under controlled solar flux provided valuable performance benchmarks for the MPSDA prototype's performance, evaluating its stability under real-world conditions is essential for practical deployment. To this end, two MPSDA units, each incorporating a larger SMVAs (100 × 100 mm), were fabricated for outdoor testing (Fig. 5a). Superhydrophilic glass fibers filaments were integrated on both sides of each device to facilitate water supply and drainage (Fig. S22). The setup was installed on the rooftop of School of Mechanical Engineering, Dalian University of Technology, and field tests were conducted on May 20, 2024. The experiment began at 8 a.m., with solar intensity and evaporation efficiency recorded hourly (Fig. 5b). As solar irradiance increased, the evaporation rate rose proportionally, peaking between 12:00 and 14:00 at approximately 900 W m^{-2}. During this peak, the evaporator achieved an evaporation rate of around 4.5 kg m^{-2} h^{-1}. Fig. 5c shows the cumulative increase in collected water volume, reaching 48 mL over 8 h. To further evaluate device performance under different weather conditions, we conducted an outdoor test on a cloudy day (Fig. S23a). Although cloudy conditions and solar flux fluctuations reduced overall performance, the multi-stage evaporator still exhibited strong outdoor productivity (Fig. S23b and Note S9). In addition, during outdoor experiments, the number of active stages in the reverse multi-stage evaporator varied between 8 and 12 due to fluctuations in ambient temperature and light intensity. To accommodate this variability, the system features a modular design that allows the number of stages to be adjusted according to the operating conditions (Fig. S24).

Ion chromatography analysis of the collected water (Fig. 5d) revealed ion concentrations well below the World Health Organization (WHO) drinking water standards. Furthermore, we measured the aluminum ion concentration in the solution. The detected concentration (0.02 mg L^{-1}) is well below the WHO drinking water standard of 0.2 mg L^{-1}. These results confirm its suitability for both drinking and agricultural use. We further verified the quality of the evaporator's freshwater output during extended operation through continuous monitoring of total dissolved solids (TDSs).[46–48] The results showed minimal fluctuation, with TDS values consistently between 30 and 40 (Fig. S25a and b), meeting standard drinking water requirements. The ion content was also analyzed after 20 days of continuous operation. Ion chromatography revealed concentrations well below WHO drinking water standards (Fig. S25c).

Long-term durability of the SMVAs is critical to the MPSDA's operational lifespan. To assess this, SMVA samples were immersed in seawater for 60 days, with evaporation performance and surface wettability measured every 15 days. Results show that after 60 days, both evaporation rate and hydrophilicity remain virtually unchanged. As shown in Fig. 5e, the SMVAs retain a stable evaporation rate of 1.3 kg m^{-2} h^{-1}, and the spreading time of a 5 μL water droplet remains consistently within 0.3 s, indicating sustained superhydrophilicity.

To protect the evaporator from environmental factors such as UV radiation, wind, and sand, we designed a three-layer shield consisting of a PLA frame, expandable polyethylene (EPE), and aluminum foil (AF) (Fig. S26). The EPE provides thermal insulation and reduces the impact of wind and

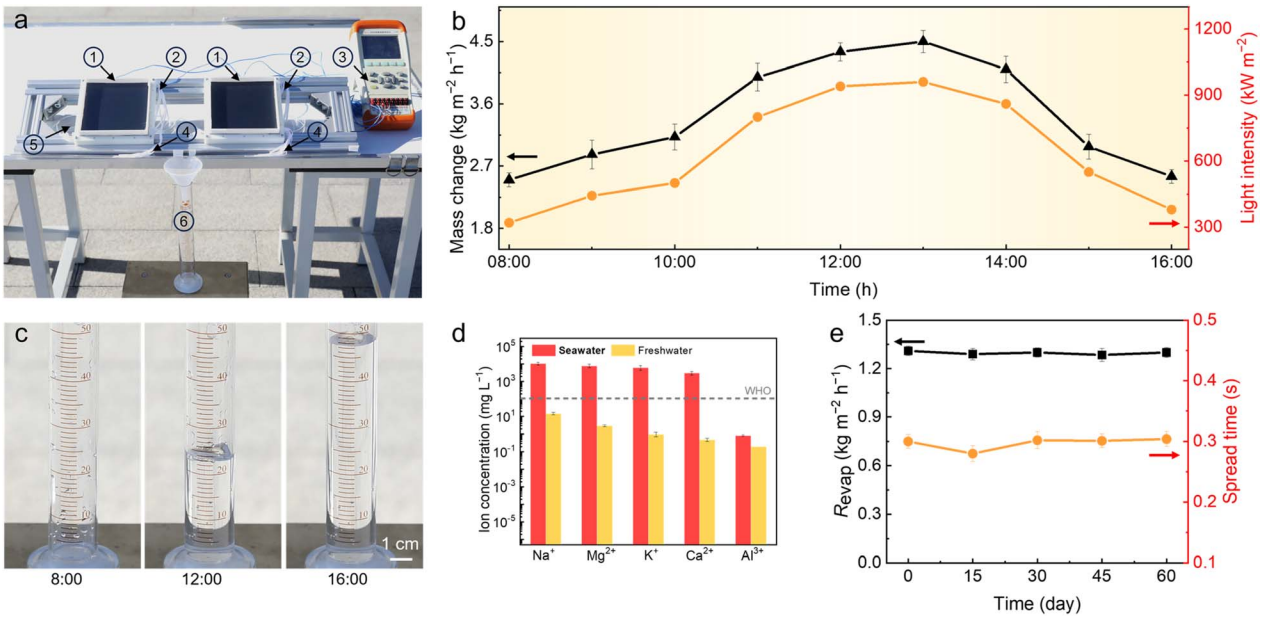

Fig. 5 Solar evaporation performance under outdoor conditions. (a) A prototype MPSDA designed to simulate practical water purification equipment. The experimental test rig consisted of (1) two multistage passive solar desalination apparatus, (2) the concentrated seawater collection devices, (3) a temperature recorder, (4) two fresh water collection devices, (5) a seawater supply device, and (6) a graduated cylinder. (b) Temporal variations in evaporation rate and solar flux. (c) Time sequences of optical images of the collected water in the graduated cylinder. (d) Ion concentration of real seawater before and after solar thermal distillation. (e) Evaporation rate and water absorption of the SMVAs after continuous immersion in seawater for more than 60 days.

sand,[49,50] while the AF enhances UV reflection.[51] Fig. S27a shows that it retained stable freshwater collection for over 20 days of continuous operation. Under cloudy conditions, it produced ~27 mL of freshwater per day, corresponding to an average productivity of 670 mL kW^{-1} h^{-1}. Under sunny conditions, production increased to ~50 mL per day, corresponding to 1.12 L kW^{-1} h^{-1}. Scanning electron microscopy (SEM) images confirmed that the SMVAs retained a porous structure after prolonged operation (Fig. S27b).

3 Experimental section

3.1 Materials

Aluminum sheet with a thickness 500 μm and superhydrophilic fiberglass paper with a thickness 200 μm were purchased from Shenzhen Universe Metal Materials Co. Ltd and Shandong Jukai technology innovation Co. Ltd, respectively. MCNT aqueous dispersion with carbon nanotube content, length and diameter of 10.6%, 10–20 μm, and ≥ 50 nm, respectively, was purchased from Beijing Boyu Hi-Tech New Material Technology Co. Ltd Titanium nitride (TiN) with particle size 20 nm was purchased from Aladdin Chemical Reagent Network. The seawater was collected from the Yellow Sea, China.

3.2 Preparation of the SMVAs

A 500 μm-thick aluminum sheet was processed using a IceFyre 1064-50 picosecond laser of 1060 nm wavelength and 200 μJ per pulse. Optimized parameters include a scan speed of 400 mm s^{-1}, interline spacing of 10 μm, and V-groove pitch of 100 μm to generate the SMVAs with optimal water absorption performance.

3.3 SMVA characterization

The microstructure of SMVAs was characterized by scanning electron microscopy (SU-5000). XPS spectra were obtained with a X-Photoelectron Spectrometer instrument (K-Alpha+). The SMVA sample was mounted onto a vertical platform and 5 μL water was dripped onto the lower end of the SMVA sample. The videos of water wetting dynamics were recorded using a digital camera. The ion concentration before and after desalination was tested using an ion chromatograph instrument (ICS-5000).

3.4 Experiments of evaporation and solar desalination

Evaporation tests were performed at a temperature of 20 ± 2 °C and a relative humidity of 45 ± 5%. Evaporation experiments under solar flux were carried out under a solar simulator (CME-sol8050-ABB) equipped with an optical filter for the standard AM 1.5-G spectrum. An analytical balance with an accuracy of 0.01 g was used to record the evaporated mass. The temperature change of surface was recorded with a contact thermometer (JK-808).

4 Conclusions

In summary, we present an innovative solar-driven reverse distillation system that synergistically combines efficient heat transfer and active salt rejection for sustainable desalination. By integrating the condensation heat exchange and hydrophilic evaporation layers onto a single aluminum plate, the height of each stage is minimized, significantly improving heat transfer efficiency. The continuous, rapid water flow within the hydrophilic layer effectively transports concentrated brine away from the evaporation interface, thereby preventing salt accumulation. Leveraging the combined benefits of high thermal conductivity and efficient salt rejection, we constructed a 15-stage multi-stage passive solar desalination apparatus. Under one sun illumination, the device achieves a high solar-to-steam conversion efficiency of 410% and a water production rate of 6.25 kg m^{-2} h^{-1}, while operating continuously for 10 hours without salt crystallization. With its combination of superior performance and demonstrated durability and cost-effective design, this work represents a significant advance in practical solar desalination solutions for water-scarce regions.

Author contributions

W. L. and Y. L. conceived the research and designed the experiments. Y. L. supervised the research. W. L., X. W., L. Z., W. G., C. L., X. B., J. C., Z. Y. carried out the experiments. W. L. and T. M. conducted the reference review and data analysis. W. L., Y. L. and S. F. prepared the manuscript. All the authors analysed the data and discussed the results.

Conflicts of interest

The authors declare that they have no competing interests.

Data availability

All data required to evaluate the conclusions of this work are provided in the main text and/or the supplementary information (SI). Additional data related to this study are available from the authors upon reasonable reque. Supplementary information: images and videos. See DOI: https://doi.org/10.1039/d5ta08988c.

Acknowledgements

This work is supported by the National Key Research and Development Program of China (2022YFB4602401), the National Natural Science Foundation of China (52475294 and 52075071), the State Key Laboratory of High-performance Precision Manufacturing (ZY202404), and the Fundamental Research Funds for the Central Universities (DUT24YG133).

Notes and references

1 K. Yang, T. Pan, N. Farhat, A. I. Felix, R. E. Waller, P. Y. Hong, J. S. Vrouwenvelder, Q. Gan and Y. Han, *Nat. Commun.*, 2024, **15**, 6260.
2 Z. Yu, Y. Li, Y. Zhang, P. Xu, C. Lv, W. Li, B. Maryam, X. Liu and S. C. Tan, *Nat. Commun.*, 2024, **15**, 6081.

3 X. Bai, E. Cui, X. Wang, L. Zhang, Z. Yuan and Y. Liu, *ACS Appl. Mater. Interfaces*, 2024, **16**, 44298–44304.
4 Z. Zhu, H. Zheng, H. Kong, X. Ma and J. Xiong, *Nat. Water*, 2023, **1**, 790–799.
5 Z. N. Garba, W. Zhou, I. Lawan, M. Zhang and Z. Yuan, *Cellulose*, 2019, **26**, 6241–6258.
6 S. W. Sharshir, A. W. Kandeal, A. Joseph, M. M. Elsayad, A. S. Abdullah, S.-H. Jang, M. Elashmawy, G. B. Abdelaziz, N. M. Ghazaly and Z. Yuan, *Appl. Therm. Eng.*, 2024, **254**, 123869.
7 Z. Liu, Z. Zhou, N. Wu, R. Zhang, B. Zhu, H. Jin, Y. Zhang, M. Zhu and Z. Chen, *ACS Nano*, 2021, **15**, 13007–13018.
8 H. Yang, Y. Sun, M. Peng, M. Cai, B. Zhao, D. Li, Z. Liang and L. Jiang, *ACS Nano*, 2022, **16**, 2511–2520.
9 H. Peng, D. Wang and S. Fu, *ACS Appl. Mater. Interfaces*, 2021, **13**, 38405–38415.
10 F. Li, N. Li, S. Wang, L. Qiao, L. Yu, P. Murto and X. Xu, *Adv. Funct. Mater.*, 2021, **31**, 2104464.
11 Z. Sun, C. Han, S. Gao, Z. Li, M. Jing, H. Yu and Z. Wang, *Nat. Commun.*, 2022, **13**, 5077.
12 X. Lin, J. Li, J. Zheng, X. Cai, L. Wang, R. Sa, C. Si, D. Jiang, Y. Kang, J. Wang, Y. Yamauchi and Z. Yuan, *Nat. Commun.*, 2025, **16**, 10818.
13 P. Liu, Y. B. Hu, X. Y. Li, L. Xu, C. Chen, B. Yuan and M. L. Fu, *Angew Chem. Int. Ed. Engl.*, 2022, **61**, e202208587.
14 L. Hou, S. Li, Y. Qi, J. Liu, Z. Cui, X. Liu, Y. Zhang, N. Wang and Y. Zhao, *ACS Nano*, 2025, **19**, 9636–9683.
15 X. Liu, F. Chen, Y. Li, H. Jiang, D. D. Mishra, F. Yu, Z. Chen, C. Hu, Y. Chen, L. Qu and W. Zheng, *Adv. Mater.*, 2022, **34**, e2203137.
16 M. Jing, W. Wang, Y. Fu, Y. Yang, W. Song and Z. Sun, *Desalination*, 2023, **564**, 116792.
17 Z. Chen, J. Wang, H. Zhou, Z. Xie, L. Shao, A. Chen, S. B. Wang and N. Jiang, *Adv. Funct. Mater.*, 2023, **33**, 2303656.
18 J. Ma, X. Sun, Y. liu, L. Wang, M. An, M. Kim, Y. Yamauchi, N. Khaorapapong and Z. Yuan, *Nano Energy*, 2025, **137**, 110781.
19 M. Chang, L. Ai, R. Yang, X. Wang, Y. Xu and J. Jiang, *Chem. Eng. J.*, 2024, **486**, 150078.
20 Y. Pang, X. Chu, L. Song, L. Jin, C. Ma, Y. Wu, L. Li, Y. Peng, X. Zheng, F. Wang, S. Wu, Z. Shen and H. Chen, *Chem. Eng. J.*, 2024, **479**, 147891.
21 Z. Zhu, H. Zheng, H. Kong, X. Ma and J. Xiong, *Nat. Water*, 2023, **1**, 790–799.
22 W. Wang, S. Aleid, Y. Shi, C. Zhang, R. Li, M. Wu, S. Zhuo and P. Wang, *Joule*, 2021, **5**, 1873–1887.
23 E. Chiavazzo, M. Morciano, F. Viglino, M. Fasano and P. Asinari, *Nat. Sustain.*, 2018, **1**, 763–772.
24 M. Morciano, M. Fasano, S. V. Boriskina, E. Chiavazzo and P. Asinari, *Energy Environ. Sci.*, 2020, **13**, 3646–3655.
25 H. Yao, P. Zhang, C. Yang, Q. Liao, X. Hao, Y. Huang, M. Zhang, X. Wang, T. Lin, H. Cheng, J. Yuan and L. Qu, *Energy Environ. Sci.*, 2021, **14**, 5330–5338.
26 S. Liu, S. Li and M. Lin, *ACS Energy Lett.*, 2023, **8**, 1680–1687.
27 D. Zhang, Y. Wan, W. Zhuang, X. Geng and P. Yang, *Chem. Eng. J.*, 2023, **466**, 143047.
28 Z. Xu, L. Zhang, L. Zhao, B. Li, B. Bhatia, C. Wang, K. L. Wilke, Y. Song, O. Labban, J. H. Lienhard, R. Wang and E. N. Wang, *Energy Environ. Sci.*, 2020, **13**, 830–839.
29 F. Wang, N. Xu, W. Zhao, L. Zhou, P. Zhu, X. Wang, B. Zhu and J. Zhu, *Joule*, 2021, **5**, 1602–1612.
30 Y. Tian, Y. Li, X. Zhang, J. Jia, X. Yang, S. Yang, J. Yu, D. Wu, X. Wang, T. Gao and F. Li, *Adv. Funct. Mater.*, 2022, **32**, 2113258.
31 X. Wang, L. Sun, Y. Shen, J. Hou, Y. Sun, B. Xiong, F. Guo, C. Li and W. Shi, *Chem. Eng. J.*, 2025, **509**, 161363.
32 Y. Yang, L. Yang, F. Yang, W. Bai, X. Zhang, H. Li, G. Duan, Y. Xu and Y. Li, *Mater. Horiz.*, 2023, **10**, 268–276.
33 Z. Yu, Y. Su, R. Gu, W. Wu, Y. Li and S. Cheng, *Nano-Micro Lett.*, 2023, **15**, 214.
34 H. Liu, M. Kim, Y. Xu, L. Jing, S. Chen, C. K. W. Lee, M. Tan, H. Zhong, Y. H. T. Chan, S. Yao and M. G. Li, *ACS Appl. Mater. Interfaces*, 2025, **17**, 30267–30283.
35 T. Bourouina, L. Royon, J. Pou and D. Beysens, *Adv. Mater.*, 2025, **37**, e2419472.
36 X. Zhao, H. Zhang, K. Y. Chan, X. Huang, Y. Yang and X. Shen, *Nano-Micro Lett.*, 2024, **16**, 222.
37 S. Ou, J. Zheng, X. Chen, R. Li, Z. Yuan, S. Liu, Y. Niu, M. An, G. Zhou, Y. Yamauchi and X. Zhang, *Energy Environ. Sci.*, 2025, **18**, 5457–5469.
38 S. C. Singh, M. ElKabbash, Z. Li, X. Li, B. Regmi, M. Madsen, S. A. Jalil, Z. Zhan, J. Zhang and C. Guo, *Nat. Sustain.*, 2020, **3**, 938–946.
39 R. R. Rye, J. A. Mann and F. G. Yost, *Langmuir*, 1996, **12**, 555–565.
40 Y. Wang, W. Zhao, Y. Lee, Y. Li, Z. Wang and K. C. Tam, *Nat. Commun.*, 2024, **15**, 6157.
41 Y. Wang, T. Wei, Y. Wang, J. Zeng, T. Wang, Q. Wang, S. Zhang, M. Zeng, F. Wang, P. Dai, X. Jiang, M. Hu, J. Zhao, Z. Hu, J. Zhu and X. Wang, *Sci. Adv.*, 2024, **10**, eadk1113.
42 M. Zou, Y. Zhang, Z. Cai, C. Li, Z. Sun, C. Yu, Z. Dong, L. Wu and Y. Song, *Adv. Mater.*, 2021, **33**, e2102443.
43 M. A. Abdelsalam, M. Sajjad, A. Raza, F. AlMarzooqi and T. Zhang, *Nat. Commun.*, 2024, **15**, 874.
44 Y. Wan, Y. Hu, H. Tu, W. Zhuang, X. Geng, T. Zhang, J. Zhang, M. Wen and P. Yang, *Small*, 2024, **20**, e2302943.
45 W. Wang, Y. Shi, C. Zhang, S. Hong, L. Shi, J. Chang, R. Li, Y. Jin, C. Ong, S. Zhuo and P. Wang, *Nat. Commun.*, 2019, **10**, 3012.
46 R. N. Brent, J. Kunkel, Z. Tomek, D. Buchardt, P. F. DeLisle and S. Sivers, *Environ. Toxicol. Chem.*, 2022, **41**, 2782–2796.
47 R. Devesa and A. M. Dietrich, *Desalination*, 2018, **439**, 147–154.
48 Z. Yuan, C. Lu, C. Liu, X. Bai, L. Zhao, S. Feng and Y. Liu, *Sci. Adv.*, 2023, **9**, eadg2352.
49 A. Pilipenko, O. Rubtsov, I. Bessonov, E. Bobrova and B. Efimov, *Mater. Today: Proc.*, 2021, **38**, 1556–1559.
50 B. Yu, X. Zhou, J. Tang, Y. Zhang and Y. Zhang, *J. Mt. Sci.*, 2024, **21**, 676–689.
51 Y. Fan, Z. Tian, F. Wang, J. He, X. Ye, Z. Zhu, H. Sun, W. Liang and A. Li, *ACS Appl. Energy Mater.*, 2021, **4**, 2932–2943.